Comparison of Electrodes for High-Performance Electrochemical Capacitors: Multi-Layer MnO$_2$/Pt and Composite MnO$_2$/Pt on Carbon Nanofibres

Yu-Jin Lee, Geon-Hyoung An, and Hyo-Jin Ahn*

*Department of Materials Science and Engineering, Seoul National University of Science and Technology,
Seoul 139-743, Korea*

Four different types of electrodes for high-performance electrochemical capacitors were prepared using electrospinning method and/or impregnation methods: (1) conventional carbon nanofibres (CNF) supports, and CNFs decorated with (2) MnO$_2$ nanophases, (3) multi-layer MnO$_2$/Pt nanophases, and (4) composite MnO$_2$ and Pt nanophases. Their morphological, structural, chemical, and electrochemical properties were characterized using field-emission scanning electron microscopy, transmission electron microscopy, X-ray diffraction, X-ray photoelectron spectroscopy, and galvanostatic charge/discharge measurements. Composite MnO$_2$ and Pt nanophases decorated on the CNFs exhibited superior capacitance ($\sim$252.3 F/g at 10 mV/s), excellent capacitance retention ($\sim$93.5% after 300 cycles), and high energy densities (13.53–18.06 Wh/kg). The enhanced electrochemical performances can be explained by the composite structure, presenting well-dispersed MnO$_2$ nanophases leading to high capacitance, and well-dispersed Pt nanophases leading to improved electrical conductivity.

Keywords: Electrochemical Capacitors, Electrospinning, Impregnation, Carbon Nanofibres, Composites.

1. INTRODUCTION

In recent decades, the limited fossil fuel resources and growing demands for portable electronic devices and electric vehicles have stimulated new research in the field of energy storage systems, such as electrochemical capacitors, Li-ion batteries, and solar cells. Compared with these systems, electrochemical capacitors possess several advantages, such as high power density (2–5 kW/kg), superb reversibility (90–95% or higher), and long cyclability ($>10^5$ cycles).[1,2] In general, the electrochemical capacitors can be classified as electrical double layer capacitors (EDLCs) and pseudocapacitors, depending on the capacitive materials and on the charge-storage mechanism. EDLCs, commonly based on carbon materials (carbon nanofibres (CNF), carbon nanotubes (CNT), and graphene) with high surface area, can store charges via reversible ion absorption at the electrode/electrolyte interface. In contrast, pseudocapacitors based on transition

metal oxides (RuO$_2$, MnO$_2$, and NiO) and conducting polymers (polyanilines, polypyrroles, and polythiophenes) involve fast and reversible redox reactions at the surface. Therefore, the specific capacitance of pseudocapacitors (typically 300–1000 F/g) is higher than that of EDLCs (typically 100–250 F/g).[3,4] Among the pseudocapacitance materials investigated to date, manganese dioxide (MnO$_2$) is a particularly promising candidate due to its high theoretical specific capacitance ($\sim$1380 F/g), low toxicity, wide voltage windows, and low cost. However, it suffers from the relatively low electrical conductivity of MnO$_2$ (10^{-5}–10^{-6} S/cm). Several problems thus have to be overcome for the development of efficient energy storage systems,[5,6] and a considerable amount of research has been devoted towards this goal. For example, Yu et al. reported a 3-D conductive wrapping method to rationally design ternary systems based on graphene/MnO$_2$/CNT and graphene/MnO$_2$/poly(3,4-ethylenedioxythiophene)-poly-(styrenesulfonate) (PEDOT:PSS) composites. The specific capacitance of the graphene/MnO$_2$/PEDOT:PSS electrodes

---

*Author to whom correspondence should be addressed.

substantially increased by $\sim$45% ($\sim$380 F/g at a current density of 0.1 mA/cm^2) compared to graphene/MnO$_2$ electrodes.[7] Also, Lee et al. reported multiwall carbon nanotube/MnO$_2$ nanocomposite ultrathin film electrodes fabricated using redox deposition. These electrodes exhibited high capacitance (246 F/cm^3 at a scan rate of 10 mV/s) and good capacity retention (up to 1000 mV/s), thanks to the rapid transport of electrons and ions within the electrodes.[8] In this study, we employed the noble Pt phases having high electrical conductivity. As a result, we used MnO$_2$–Pt as a starting material for high-performance electrochemical capacitors. To date, no systematic studies have appeared on MnO$_2$ electrodes, in particular comparing the performance of CNFs decorated with MnO$_2$ nanophases, multi-layer MnO$_2$/Pt nanophases, and composite MnO$_2$ and Pt nanophases.

In the present study, we designed and synthesized four types of electrodes using electrospinning and/or impregnation methods. CNFs were chosen as electrode supports for charge transport, and Pt was used as additive to improve the electrical conductivity of MnO$_2$.

2. EXPERIMENTAL DETAILS

We prepared four types of electrodes to assess their performance as electrochemical capacitors:
(1) conventional CNFs,
(2) CNFs decorated with MnO$_2$ nanophases,
(3) CNFs decorated with multi-layer MnO$_2$/Pt nanophases, and
(4) CNFs decorated with composite MnO$_2$ and Pt nanophases.

These four types of electrodes are hereafter referred to as conventional CNFs, sample A, sample B, and sample C, respectively. First, the conventional CNFs, used as electrode supports of samples A, B, and C, were synthesized using an electrospinning method. In the electrospinning solution, polyacrylonitrile (PAN, M$_w$ = 150,000 g/mol, Aldrich) and poly(vinylpyrrolidone) (PVP, M$_w$ = 1,300,000 g/mol, Aldrich) were dissolved in N,N-Dimethylformamide (DMF, Aldrich) for 5 h at room temperature. The mixture solution was placed in a syringe equipped with a 23 gauge stainless steel needle. During the electrospinning process, the feeding rate and the needle collector (aluminum foil) distance were fixed to $\sim$0.03 ml/h and $\sim$15 cm, respectively, under a fixed voltage of $\sim$13 kV. The as-spun nanofibres were stabilized at 280 °C for 2 h in air atmosphere and then carbonized at 800 °C for 2 h in N$_2$ atmosphere. Then, an impregnation method was employ to synthesize the CNFs decorated with MnO$_2$ nanophases (sample A). Before impregnation, the CNFs were dispersed in a mixed solution of nitric acid and hydrofluoric acid (1:1 volume ratio) for 5 h, in order to form functional groups such as –COOH, –OH, and >C=O at the edge surface.[9, 10] The functionalized CNFs were then dispersed in de-ionized (DI) water for

1 h, after which 0.56 mM manganese(II) acetate tetrahydrate (C$_4$H$_6$MnO$_4 \cdot$4H$_2$O, Aldrich) was added and stirred for 1 h, while continuously adding sodium borohydride (NaBH$_4$, Aldrich) reducing agent to the mixture solution. After the reduction reactions, the resultant samples were washed several times and freeze-dried by liquid N$_2$. A two-step impregnation method was used to synthesize the CNFs decorated with the multi-layer MnO$_2$/Pt nanophases (sample B). The A samples were dispersed in DI water, and the previous impregnation process was repeated using 0.14 mM chloroplatinic acid hydrate (H$_2$PtCl$_6 \cdot x$H$_2$O, Aldrich) instead of manganese(II) acetate tetrahydrate. Finally, a co-impregnation method was used to synthesize the CNFS decorated with the composite MnO$_2$ and Pt nanophases (sample C). To synthesize this system, the functionalized CNFs were dispersed in DI water for 1 h. Then, 0.56 mM manganese(II) acetate tetrahydrate (C$_4$H$_6$MnO$_4 \cdot$4H$_2$O, Aldrich) and 0.14 mM chloroplatinic acid hydrate were added simultaneously and stirred for 1 h, and the above-mentioned processes were repeated. The amount of Mn precursor on the CNFs and the Mn/Pt precursor molar ratio were controlled to be 20 wt% and 8:2, respectively.

Morphological and structural properties of the samples were performed by field-emission scanning electron microscopy (FESEM, Hitachi S-4800) and a transmission electron microscopy (MULTI/TEM, Tecnai G^2, KBSI Gwangju Center). The crystallinity of the samples was investigated by X-ray diffraction (XRD, Rigaku D/Max 2500 V). The chemical bonding states of the samples were characterized by X-ray photoelectron spectroscopy (XPS, ESCALAB 250) equipped with an Al Kα X-ray source. The electrochemical measurements of the samples were obtained by a potentiostat/galvanostat (PGST302N, Eco Chemie) with a three-electrode cell system in a 0.5 M H$_2$SO$_4$ electrolyte. The three-electrode cell system consisted of a glassy carbon electrode (7.06 mm^2 surface area, CH Instruments) as working electrode, Pt wire as counter electrode, and Ag/AgCl as reference electrode. Electrode materials were fabricated by mixture pastes composed of 70 wt% as-prepared samples, 20 wt% acetylene black, and 10 wt% polyvinylidene fluoride (PVDF) binder in N-methyl-2-pyrrolidinone (NMP). The pastes were coated on the glassy carbon working electrode and dried at 80 °C. Cyclic voltammograms (CVs) were determined at scan rates of 10, 30, 50, 100, and 200 mV/s in a 0.0–1.0 V potential range versus Ag/AgCl (saturated KCl). In addition, the galvanostatic charge/discharge of all samples was measured using a two-electrode system in 6 M KOH electrolyte. The working electrodes were prepared on Ni foam (1 cm $\times$ 1 cm). Galvanostatic charge/discharge measurements were performed at current densities from 0.2 to 20 A/g in a potential range of 0.0–1.0 V. The electrical properties of the samples were measured using Hall Effect Measurement System (Ecopia, HMS-3000).

3. RESULTS AND DISCUSSION

Figure 1 shows the FESEM images obtained for (a) the conventional CNFs, (b) sample A, (c) sample B, and (d) sample C, respectively. All samples exhibited uniform nanofibres and formed a network structure. The average diameters of the samples were in the approximate ranges of 215–272 nm for the conventional CNFs, 214–280 nm for sample A, 210–279 nm for sample B, and 221–293 nm for sample C. As shown in Figure 1, the conventional CNFs exhibited a smooth surface, whereas samples A, B and C exhibited rough surfaces due to the presence of MnO_2 nanophases (sample A), multi-layer MnO_2/Pt nanophases (sample B), and composite MnO_2 and Pt nanophases (sample C) decorated on the CNF supports. In particular, the extent of aggregation in sample B was higher than in sample C.

Figures 2(a)–(d) show high-resolution TEM images of conventional CNFs, samples A, B, and C, respectively, with the insets displaying the corresponding low-resolution TEM images. The conventional CNFs showed a uniform bright contrast across the whole sample (Fig. 2(a)). In contrast, sample A (Fig. 2(b)) exhibited nano-sized spots, reflecting formation of MnO_2 nanophases of 40–125 nm size on the CNFs. Furthermore, multi-layer structures of MnO_2 and Pt nanophases decorated with the CNFs were detected on sample B (Fig. 2(c)). In the case of sample C, the TEM images highlight that a composite of well-dispersed MnO_2 and Pt nanophases was formed on the CNF supports, as shown in Figure 2(d). The MnO_2 and Pt nanophases showed much more limited aggregation, in the size range of 14–41 nm and 2–4 nm, respectively. This may be an indication that the Pt addition in composites prevents the aggregation of MnO_2 and Pt nanophases during the co-impregnation process. Thus, the composite of
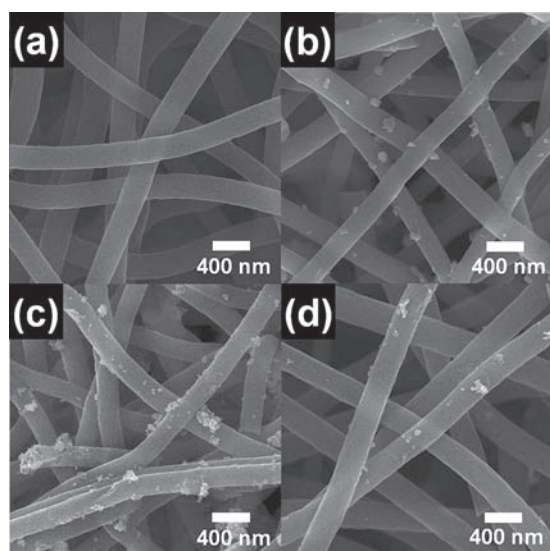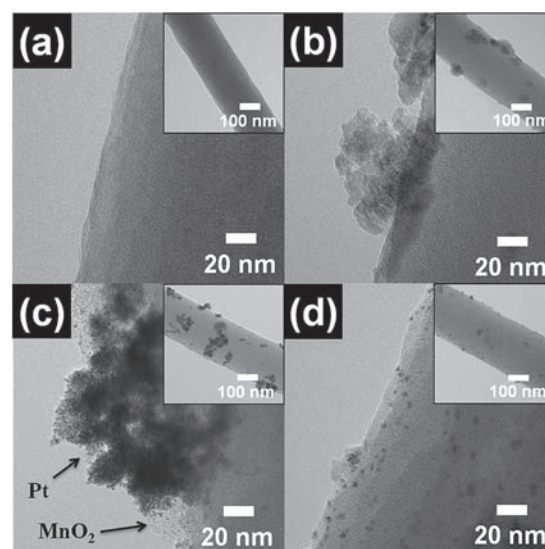

Figure 2. TEM images obtained from (a) conventional CNFs, (b) sample A, (c) sample B, and (d) sample C.

MnO_2 and Pt nanophases on the CNFs obtained using the co-impregnation method exhibited higher dispersion than the multi-layer MnO_2/Pt nanophases synthesized with the two-step impregnation method.

Figure 3 shows the XRD patterns of all samples. The broad diffraction peak at 25° in the conventional CNFs pattern corresponds to the (002) graphite layers. The main diffraction peak of samples A, B, and C occurs at 19.1°, corresponding to the (111) planes of the face-centered cubic (fcc) structure (space group Fm3m [227], JCPDS card No. 44-0992) of the λ-MnO_2 nanophase. Samples B and C also presented the diffraction peaks of polycrystalline Pt phases at 39.7° and 46.2°, corresponding to (111) and (200) planes of the fcc structure (space group Fm3m [225], JCPDS card No. 04-0802). In particular, for sample C, the intensities of the MnO_2 and Pt nanophases peaks at 19.1° and 39.7° were lower than those of sample B, due to the smaller average particle size of the MnO_2 and Pt
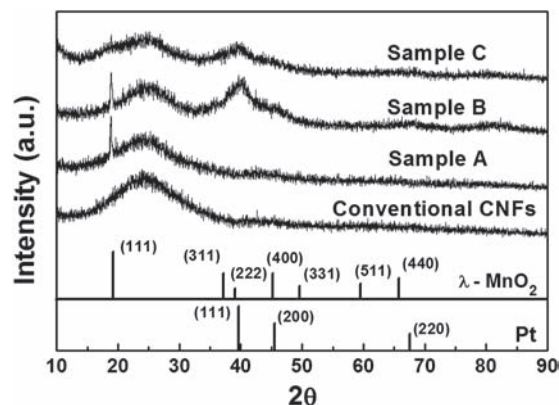

Figure 1. FESEM images obtained from (a) conventional CNFs, (b) sample A, (c) sample B, and (d) sample C.

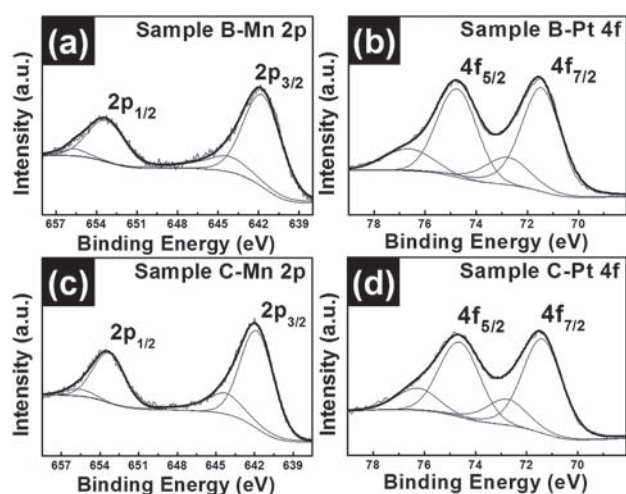**Figure 3.** XRD patterns of all samples.

Figure 4. XPS core-level spectra for Mn $2p$ and Pt $4f$ obtained from samples B and C.

nanophases.[11] This is in good agreement with the results obtained by examining the TEM images.

XPS analyses were performed to identify the chemical bonding states of Mn and Pt. The XPS spectra corresponding to the Mn $2p$ and Pt $4f$ core levels of samples B and C are shown in Figures 4(a)–(d). In the Mn $2p$ spectra, the signals of the Mn $2p_{3/2}$ and Mn $2p_{1/2}$ photoelectrons of samples B and C were observed at ~641.7 eV and ~653.0 eV, corresponding to Mn(IV) states in the MnO_2 phases. Additional minor peaks at higher binding energies of ~644.2 eV and ~655.5 eV correspond to hydroxyl

groups on the surface of Mn nanophases.[12, 13] Furthermore, the signals of the Pt $4f_{7/2}$ and Pt $4f_{5/2}$ photoelectrons of samples B and C were observed at ~74.7 eV and ~71.3 eV, indicating the presence of elemental Pt in metallic Pt phases. Other minor peaks at ~76.8 eV and 73.2 eV denoted Pt(II) states, implying the presence of PtO and Pt(OH)$_2$ on the surface of the Pt phases.[14] This is because, generally, the nano-sized particles are metastable, owing to their high surface area to volume ratio, so that the surfaces of Mn and Pt nanophases are more readily oxidized during a synthetic process, or upon air exposure.[15] The FESEM, TEM, XRD, and XPS data thus confirm that we successfully synthesized the four different types of electrodes targeted.

Electrochemical measurements were performed using a three-electrode configuration in a 0.5 M H_2SO_4 electrolyte. Figures 5(a)–(d) display cyclic voltammograms (CVs) for conventional CNFs and samples A, B, and C, respectively. All samples were evaluated at scan rates 10, 30, 50, 100, and 200 mV/s in a potential range of 0.0–1.0 V (versus Ag/AgCl). As the scan rate increased, the area under the CV curve of all samples gradually increased with decreasing specific capacitance, which is a very common effect, mainly caused by diffusion limitation of electrolyte ions.[16] In particular, the CVs of conventional CNFs displayed a nearly rectangular shape even at a high scan rate of 200 mV/s, indicating EDLC capacitive behavior in both directions of the potential scanning. Figure 5(e) shows the CVs of all samples obtained at a scan rate of 10 mV/s in the potential range of 0.0–1.0 V versus
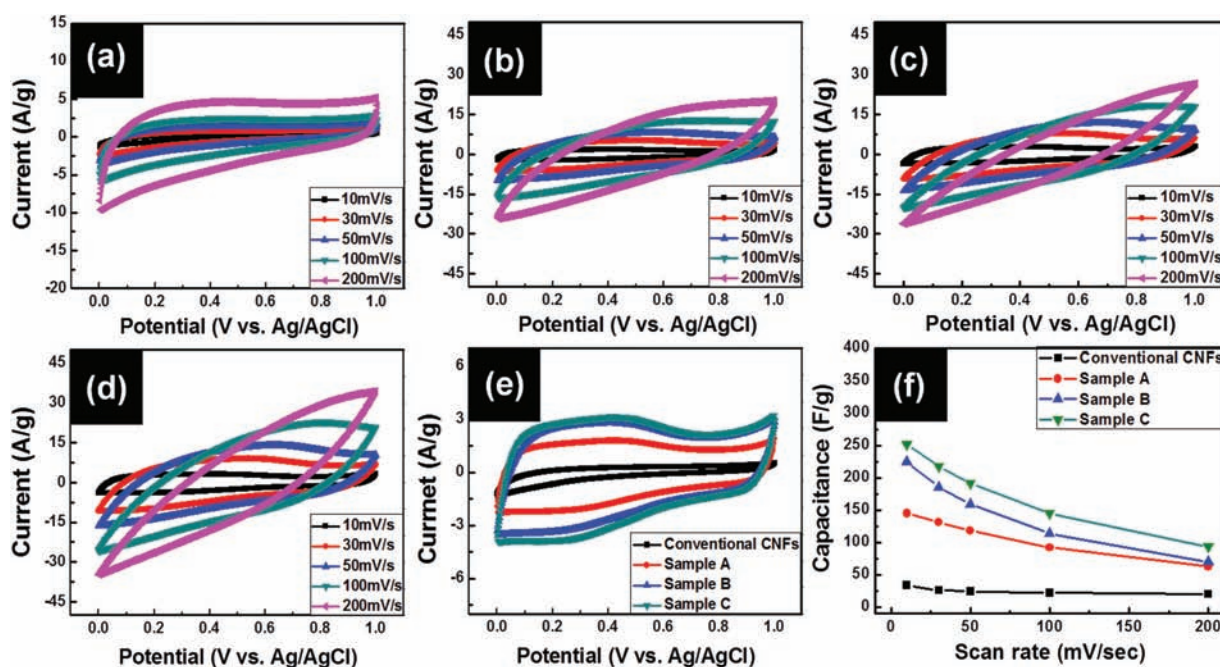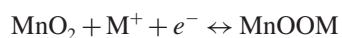

Figure 5. Cyclic voltammograms of (a) conventional CNFs, (b) sample A, (c) sample B, and (d) sample C at scan rates of 10, 30, 50, 100, and 200 mV/s in the potential range of 0.0–1.0 V. (e) Cyclic voltammograms of all samples measured at a scan rate of 10 mV/s. (f) Capacitance estimated as a function of a potential scan rate.

Ag/AgCl. Pseudocapacitive behavior was observed around 0.4 V, which can be explained by the faradaic redox reactions involving the MnO_2 phases. The reversible redox reactions of the Mn ion in a pseudocapacitor can be exploited for charge storage according to the following mechanism:[17]

$$MnO_2 + M^+ + e^- \leftrightarrow MnOOM$$

where M^+ presents protons (H_3O^+) or alkali cations in the electrolyte. Figure 5(f) shows the specific capacitances of all samples at various scan rates, as estimated from Figures 5(a)–(d). The specific capacitances (C) in three-electrode configuration were calculated based on the following equation:[18, 19]

$$C = (Q_a + Q_c)/(2m\Delta V) \tag{1}$$

where Q_a and Q_c are the charges obtained by the anodic and cathodic integrated areas of the CVs, respectively, whereas m and ΔV denote the mass of the active materials and the potential range of the CVs, respectively. The specific capacitances of conventional CNFs and of samples A, B, and C estimated from Eq. (1) were $\sim$33.6 F/g, $\sim$145.1 F/g, $\sim$224.4 F/g, and $\sim$252.3 F/g at 10 mV/s, respectively. Sample C displayed excellent capacitance performance in comparison to other samples. In particular, the value estimated for sample C is $\sim$7.5 times higher than that of the conventional CNFs and $\sim$1.7 times higher than that of sample A. These improved electrochemical performances are due to the formation of well-dispersed MnO_2 and Pt nanophases decorated on the CNFs.

To further evaluate the electrochemical performance of all samples, galvanostatic charge/discharge curves were measured via two-electrode configuration in 6 M KOH electrolyte. Figure 6(a) shows the galvanostatic charge/discharge curves of conventional CNFs, sample B, and sample C. The CV curves of the samples exhibited a nearly symmetric triangular shape, indicating excellent electrochemical reversibility of the electrodes. The discharge time of the samples were $\sim$16 s for conventional CNFs, $\sim$46 s for sample B, and $\sim$64 s for sample C,

indicating that sample C exhibited the best capacitance behavior at a current density of 0.5 A/g. In addition, the cycling properties of sample C measured at current density of 1 A/g are shown in Figure 6(b). It can be noted that $\sim$93.5% of the initial capacitance was retained after 300 cycles, showing that sample C has superior capacitance and cyclability. Figure 6(c) shows Ragone plots of conventional CNFs, sample B, and sample C determined by energy density (E) and power density (P). The energy density and power density were calculated from the galvanostatic charge/discharge curves according to the following equations:[20, 21]

$$C_{sp} = 4I/(m\Delta V/t) \tag{2}$$
$$E = C_{sp}V^2/8 \tag{3}$$
$$P = E/t \tag{4}$$

where I, m, ΔV, and t are the current of discharge, total mass of the active materials in both electrodes, potential difference during discharge voltage, and discharge time, respectively. The Ragone plots of the samples were plotted after varying the current density from 0.2 A/g to 10 A/g. Sample C exhibited superb electrochemical properties with maximum energy density of $\sim$18.0 Wh/kg (at a power density of $\sim$396.4 W/kg) and power density of $\sim$18 kW/kg (at an energy density of $\sim$13.5 Wh/kg). The electrical property of the samples was investigated using Hall Effect Measurement. The electrical conductivities of the conventional CNFs, sample A, sample B, and sample C are $\sim$2.7 $\times$ 10^{-1} S/cm, $\sim$1.5 $\times$ 10^{-1} S/cm, $\sim$2.9 $\times$ 10^{-1} S/cm, and $\sim$3.8 $\times$ 10^{-1} S/cm, respectively. Thus, sample C shows highest electrical conductivity among other samples. These excellent electrical properties of sample C are attributed to the composite structure consisting of well-dispersed MnO_2 and Pt nanophases decorated on the CNFs. Such excellent electrochemical properties can be attributed to two main factors. The first is that the relatively low electrical conductivity of MnO_2 phases can lead to poor capacitive performance. Therefore, the presence of Pt nanophases in samples B and C improved electrical conductivity, resulting in higher reversible capacitance.[22]
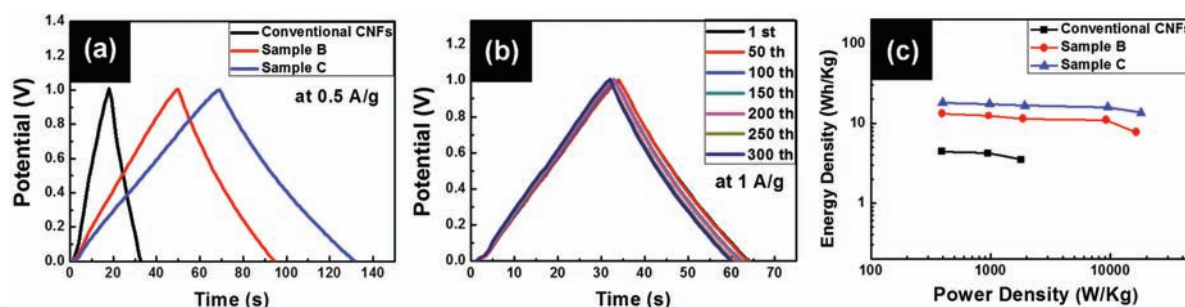

Figure 6. (a) Galvanostatic charge/discharge curves of conventional CNFs, sample B, and sample C at current density 0.5 A/g in the range 0.0–1.0 V. (b) Charge/discharge curves after 300 cycles for sample C. (c) Ragone plots for conventional CNFs, sample B, and sample C measured in 6 M KOH electrolyte.

The other factor is that the pseudocapacitance is proportional to the surface area of MnO_2 nanophases, with larger surface areas leading to improved electro-redox (faradaic) reactions. Thus, composites of MnO_2 and Pt nanophases decorated on the CNFs (as in sample C) have an enhanced electroactive surface area compared to multi-layer MnO_2/Pt nanophases (sample B) owing to the presence of well-dispersed MnO_2 and Pt nanophases.[23, 24] Therefore, the performance improvements, including enhanced capacitance, energy/power densities, and cyclability, can be attributed to the presence on the CNFs of composites of well-dispersed MnO_2 nanophases with high capacitance, and of Pt nanophases with improved electrical conductivity.

4. CONCLUSIONS

Four types of electrodes were successfully synthesized. The electrodes involving composites of MnO_2 and Pt nanophases decorated on the CNFs (sample C) were synthesized using electrospinning and co-impregnation methods. This type of electrodes showed excellent electrochemical properties, including high capacitance ($\sim$252.3 F/g at 10 mV/s), high energy densities (13.53–18.06 Wh/kg), good cycling stability ($\sim$93.5% retention of initial capacitance), and high electrical conductivity ($\sim$3.8 × 10^{-1} S/cm) compared to the other electrodes tested. This improved electrochemical performance can be attributed to the effect of well-dispersed MnO_2 and Pt nanophases decorated on the CNFs, as well as to the presence of Pt nanophases. Therefore, composite MnO_2 and Pt nanophases decorated on CNFs may represent a promising type of electrodes for high-performance electrochemical capacitors.

References and Notes

1. Q. T. Qu, Y. Shi, S. Tian, Y. H. Chen, Y. P. Wu, and R. Holze, *J. Power Sources* 194, 1222 (**2009**).
2. Y. Zhang, H. Feng, X. Wu, L. Wang, A. Zhang, T. Xia, H. Dong, X. Li, and L. Zhang, *Int. J. Hydrogen Energy* 34, 4889 (**2009**).
3. G. Yu, X. Xie, L. Pan, Z. Bao, and Y. Cui, *Nano Energy* 2, 213 (**2013**).
4. A. G. Pandolfo and A. F. Hollenkamp, *J. Power Sources* 157, 11 (**2006**).
5. M. Zhi, A. Manivannan, F. Meng, and N. Wu, *J. Power Sources* 208, 345 (**2012**).
6. X. Lu, M. Yu, G. Wang, T. Zhai, S. Xie, Y. Ling, Y. Tong, and Y. Li, *Adv. Mater.* 25, 267 (**2013**).
7. G. Yu, L. Hu, N. Liu, H. Wang, M. Vosgueritchian, Y. Yang, Y. Cui, and Z. Bao, *Nano Lett.* 11, 4438 (**2011**).
8. S. W. Lee, J. Kim, S. Chen, P. T. Hammond, and Y. Shao-Horn, *ACS Nano* 4, 3889 (**2010**).
9. H. P. Boehm, *Carbon* 32, 759 (**1994**).
10. T. Maiyalagan, *Int. J. Hydrogen Energy* 34, 2874 (**2009**).
11. H.-J. Ahn, H.-C. Choi, K.-W. Park, S.-B. Kim, and Y.-E. Sung, *J. Phys. Chem. B* 108, 9815 (**2004**).
12. M. A. Kostowskyj, D. W. Kirk, and S. J. Thorpe, *Int. J. Hydrogen Energy* 35, 5666 (**2010**).
13. Y. Wang, G. Yang, Z. Yang, L. Zhang, M. Fu, H. Long, Z. Li, Y. Huang, and P. Lu, *Electrochim. Acta* 102, 416 (**2013**).
14. B. P. Vinayan and S. Ramaprabhu, *Nanoscale* 5, 5109 (**2013**).
15. Y. Lee, J.-R Choi, K. J. Lee, N. E. Stott, and D. Kim, *Nanotechnology* 19, 415604 (**2008**).
16. W. Xing, S. Z. Qiao, R. G. Ding, F. Li, G. Q. Lu, Z. F. Yan, and H. M. Cheng, *Carbon* 44, 216 (**2006**).
17. G.-R. Li, Z.-P. Feng, Y.-N. Ou, D. Wu, R. Fu, and Y.-X. Tong, *Langmuir* 26, 2209 (**2010**).
18. C. Zheng, L. Qi, M. Yoshio, and H. Wang, *J. Power Sources* 195, 4406 (**2010**).
19. G.-H. An and H.-J. Ahn, *ECS Solid State Lett.* 2, M33 (**2013**).
20. M. Liu, W. W. Tjiu, J. Pan, C. Zhang, W. Gao, and T. Liu, *Nanoscale* 6, 4233 (**2014**).
21. X. Li, W. Xing, S. Zhuo, J. Zhou, F. Li, S.-Z. Qiao, and G.-Q. Lu, *Bioresource. Technol.* 102, 1118 (**2011**).
22. H.-J. Ahn and T.-Y. Seong, *J. Alloy. Compd.* 478, L8 (**2009**).
23. C. Yuan, L. Chen, B. Gao, L. Su, and X. Zhang, *J. Mater. Chem.* 19, 246 (**2009**).
24. R.-R. Bi, X.-L. Wu, F.-F. Cao, L.-Y. Jiang, Y.-G. Guo, and L.-J. Wan, *J. Phys. Chem. C* 114, 2448 (**2010**).